 CMES, vol.92, no.6, pp.573-594, 2013

Coupled PIEM/FEM Algorithm Based on Mindlin-Reissner Plate Theory for Bending Analysis of Plates with Through-Thickness Hole

De-Shin Liu[1], **Chin-Yi Tu**[1], **and Cho-Liang Chung**[2]

Abstract: The Infinite Element Method (IEM) is widely used for the analysis of elastostatic structures containing singularities. In the IEM method, the problem domain is partitioned into multiple element layers, where the stiffness matrix of each layer is similar to that of the other layers in the discretized domain. However, in Mindlin-Reissner plate theory, the stiffness matrix varies through the layers of the plate, and thus the conventional IEM algorithm cannot be applied. Accordingly, the present study proposes a Plate Infinite Element Method (PIEM) in which the element stiffness matrix is separated into two sub-matrices; each being similar to the equivalent sub-matrix of the element layers above and below it. The validity of the proposed algorithm is demonstrated by comparing the results obtained for the deflection contour of a plate under four-point bending with those obtained using conventional ABAQUS Finite Element Method (FEM) software. The PIEM algorithm is then coupled with an FEM algorithm and used to investigate the effects of the hole size, hole position and hole profile / area on the bending strength (S_b) of plates containing through-thickness holes. In general, the results show that the combined PIEM/FEM algorithm provides an accurate and computationally efficient means of analyzing the bending behavior of plates containing through-thickness holes.

Keywords: IEM, FEM, Mindlin-Reissner plate theory, Four-point bending test, through-thickness hole.

1 Introduction

A large number of structural components in engineering can be classified as plates. Plates with through-thickness holes are used in many civil, mechanical, biome-

[1] Advanced Institute of Manufacturing for High-tech Innovations and Department of Mechanical Engineering, National Chung Cheng University, 168, University Rd., Min-Hsiung, Chia-Yi, 621, Taiwan, R.O.C.

[2] Department of Materials Science and Engineering, I-Shou University, No. 1, section 1, Shiuecheng Road, Dashu Shiang, Kaohsiung Country, Taiwan, 840, R.O.C.

chanical and aeronautical structures as a means of adapting the flexural rigidity of the structure or interconnecting the various structural members [Yamamoto, Hongo, Berglund, Sperling, Cofield, An, and Steinmann (in press)]. As a result, the bending characteristics of plates containing opening holes have attracted significant attention in the literature for obtaining the design objectives of such structures. Various methods are available for measuring the flexural rigidity of such plates, including the three-point bending test (3PB), the four-point bending test (4PB), the ring-on-ring test, and the ball-on-ring test [Feraboli and Kedward (2003); Huurman, Gelpke, and Jacobs (2012)]. In the 4PB test, the plate is in a state of pure bending and thus the 4PB test is considered to be the most reliable method for estimating the relationship between the bending moment and the deflection. In performing the 4PB test, the flexural stiffness per unit width of the plate (S_b) [Lee and Park (2004)] is defined as

$$S_b = \frac{EI}{W} = \frac{ML^2}{8\omega_{\max} W} \tag{1}$$

where E is the Young's Modulus, I is the moment of inertia, M is the bending moment, L is the length of the plate, W is the width of the plate, and $\omega_{\max}$ is the maximum deflection of the plate.

The literature contains many numerical investigations into the mechanical response of plates subjected to various types of loading. For example, many researchers have examined the out-of-plane bending of finite thickness plates containing a circular hole using the Finite Element Method (FEM) [Komur and Sonmez (2008); Yu, Guo, She, and Zhao (2008); Yang, Kim, Cho, and Beom (2008); Maiorana, Pellegrino, and Modena (2009); Park, Kim, Kwon, and Chung (2012)]. Other researchers have investigated the bending response of elastostatic plates containing singularities using the Boundary Element Method (BEM) [Chen, Shen, and Chen (2006); Chen, Hsiao, and Leu (2006); Lee, Chen, and Lee (2007); Dong, Lo, and Cheung (2004)]. In addition, various researchers have analyzed the static and free vibration responses of complex-shaped plates using the Mesh-Free Method (MFM) [Liu and Chen (2001); Kee, Liu, and Lu (2008)]. However, in the FEM, BEM and MFM methods, a re-modeling process is required to evaluate the effects on the bending response of changes in the properties of the singularity (e.g., the hole size, hole number, hole position, and so on). As a result, such methods, while highly accurate, are time consuming and inefficient.

The Infinite Element Method (IEM) provides an alternative approach for solving singularity-type engineering problems. In essence, the IEM approach involves discretizing the problem domain into a predefined number of element layers in such a way that the stiffness matrix of each layer is similar to that of all the other layers in

the domain. Ying [Ying (1992, 1995)] proved the existence of a transformation matrix which relates the nodal displacement vectors of the inner and outer layers and showed that the total stiffness matrix of the body under consideration can therefore be degenerated to form a combined stiffness matrix relating only to the boundary nodes and tractions. Liu proposed a two-dimensional hybrid IEM/FEM scheme for analyzing various types of elastic and singularity problems [Liu and Chiou (2003, 2004); Liu, Tu, and Chung (2012)]. However, the IEM algorithm cannot be applied directly to Mindlin-Reissner bending problems due to the incompatible differential order of the shear stiffness component.

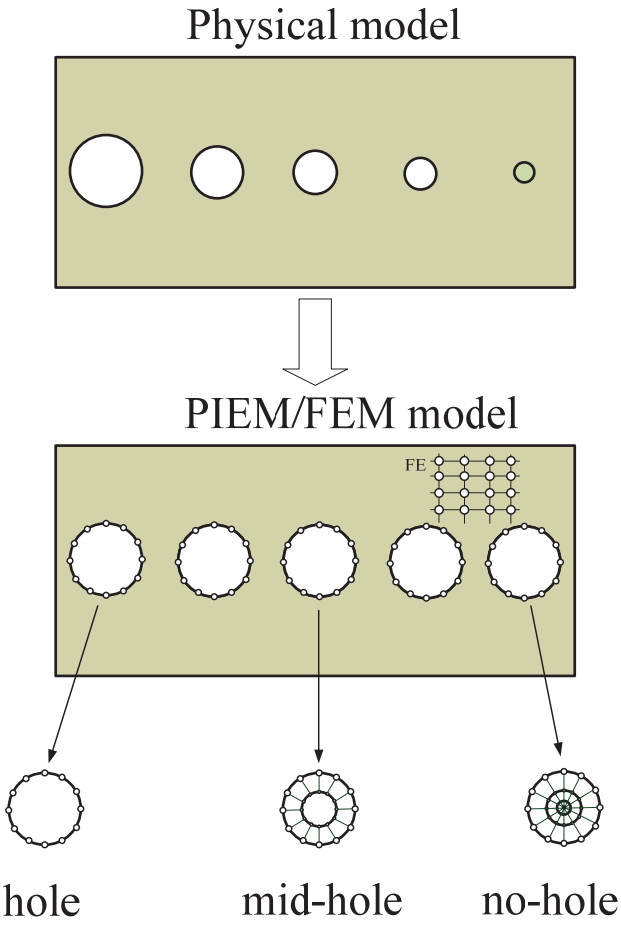

Figure 1: Physical and PIEM/FEM models of rectangular plate containing through-thickness holes

Accordingly, the present study proposes a Plate IEM (PIEM) algorithm based on Mindlin-Reissner theory in which the conventional IEM element stiffness matrix is decomposed into two sub-matrixes, where each sub-matrix is similar to the equivalent sub-matrix of all the other element layers in the discretized domain. The validity of the proposed PIEM algorithm is confirmed by comparing the numerical results obtained for the 4PB deflection of a plate with those obtained using commercial FEM software (ABAQUS). The PIEM algorithm is then integrated with a FEM scheme in order to evaluate the bending response of plates containing through-thickness holes with various sizes, positions and profiles / areas. In the proposed PIEM/FEM algorithm, the region of the plate containing the through-thickness hole is modeled using the PIEM scheme, while the remainder of the computational domain is meshed using the conventional FEM scheme (see Fig. 1). As a result, in evaluating the effect on the plate stiffness of changes in the diameter, position and profile / area of the through-thickness hole, it is necessary only to re-mesh the PIEM region of the domain. Consequently, the numerical efficiency of the solution procedure is significantly improved.

2 Mindlin-Reissner plate theory

Mindlin-Reissner plate theory is an extension of Kirchhoff-Love plate theory which takes into account shear deformations through the thickness of the plate [Mindlin (1951); Wang, Lim, Reddy, and Lee (2001)]. In applying Mindlin-Reissner theory, the following assumptions are imposed: (a) the thickness of the plate is unchanged during deformation; (b) the normal stress through the thickness can be ignored; and (c) the normal line of the thickness is perpendicular to the neutral axis line following deformation [Nguyen-Xuan, Rabczuk, Bordas, and Debongnie (2008); Cui, Liu, and Li (2010)].

Given the assumptions above, the full three-dimensional solid mechanics problem reduces to a two-dimensional problem. Therefore, the in-plane displacements are given as shown in Eqs. (2) and (3), respectively, while the transverse displacement has the form given in Eq. (4).

$$u = -z\theta_x(x,y) = -z\left(\frac{\partial \omega}{\partial x} - \gamma_{xz}\right) \tag{2}$$

$$v = -z\theta_y(x,y) = -z\left(\frac{\partial \omega}{\partial y} - \gamma_{yz}\right) \tag{3}$$

$$\omega = \omega(x,y) \tag{4}$$

where θ_x and θ_y are the rotations of the mid-plane about the y- and x- axes, respectively; and γ is the angle caused by the transverse shear deformation. Figure 2 shows the free body diagram of the plate element, where the degrees of freedom of each node in the plate element are transferred from $[u, v, \omega]$ to $[\theta_x, \theta_y, \omega]$.

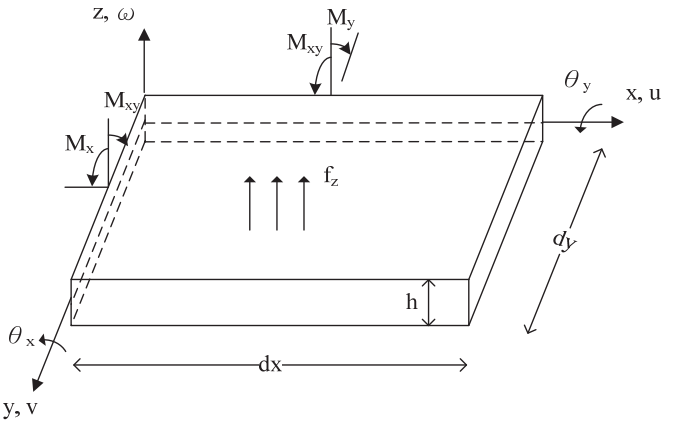

Figure 2: Free-body diagram of plate element

The 4-node-plate finite element stiffness matrix can be derived by Mindlin-Reissner theory and mapping the physical coordinates to the natural coordinates. The associated plate stiffness is given by Eq. (5), in which k_b is the bending stiffness and k_s is the shear stiffness. Note that the plate material is assumed to be linear elastic, isotropic, and homogenous. The resultant equation of each element has the form shown in Eq. (12).

$$k = k_b + k_s \tag{5}$$

where

$$k_b = \frac{h^3}{12} \int_{-1}^{1}\int [B_b]^T [D_b][B_b] \det|J|\, d\zeta\, d\eta \tag{6}$$

$$k_s = h\kappa \int_{-1}^{1}\int [B_s]^T [D_s][B_s] \det|J|\, d\zeta\, d\eta \tag{7}$$

in which h is the thickness of the plate, κ is the shear energy correction factor (usually equal to 5/6), and J is the Jacobian matrix.

$$[B_b] = \begin{bmatrix} \frac{\partial H_1}{\partial x} & 0 & 0 & \frac{\partial H_2}{\partial x} & 0 & 0 & \frac{\partial H_3}{\partial x} & 0 & 0 & \frac{\partial H_4}{\partial x} & 0 & 0 \\ 0 & \frac{\partial H_1}{\partial y} & 0 & 0 & \frac{\partial H_2}{\partial y} & 0 & 0 & \frac{\partial H_3}{\partial y} & 0 & 0 & \frac{\partial H_4}{\partial y} & 0 \\ \frac{\partial H_1}{\partial y} & \frac{\partial H_1}{\partial x} & 0 & \frac{\partial H_2}{\partial y} & \frac{\partial H_2}{\partial x} & 0 & \frac{\partial H_3}{\partial y} & \frac{\partial H_3}{\partial x} & 0 & \frac{\partial H_4}{\partial y} & \frac{\partial H_4}{\partial x} & 0 \end{bmatrix} \tag{8}$$

where H_i is a 4-node plate finite element shape function.

$$[D_b] = \frac{E}{1-v^2} \begin{bmatrix} 1 & v & 0 \\ v & 1 & 0 \\ 0 & 0 & \frac{1-v}{2} \end{bmatrix} \tag{9}$$

where E is the Young's Modulus of the plate and v is the Poisson ratio.

$$[B_s] = \begin{bmatrix} -H_1 & 0 & \frac{\partial H_1}{\partial x} & -H_2 & 0 & \frac{\partial H_2}{\partial x} & -H_3 & 0 & \frac{\partial H_3}{\partial x} & -H_4 & 0 & \frac{\partial H_4}{\partial x} \\ 0 & -H_1 & \frac{\partial H_1}{\partial y} & 0 & -H_2 & \frac{\partial H_2}{\partial y} & 0 & -H_3 & \frac{\partial H_3}{\partial y} & 0 & -H_4 & \frac{\partial H_4}{y} \end{bmatrix} \tag{10}$$

$$[D_s] = \begin{bmatrix} G & 0 \\ 0 & G \end{bmatrix}$$
$$G = \frac{E}{2(1+v)} : \text{ shear modulus} \tag{11}$$

$$\left[\frac{h^3}{12} \int_{-1}^{1}\int_{-1}^{1} [B_b]^T [D_b][B_b] \det|J|\, d\zeta\, d\eta + h\kappa \int_{-1}^{1}\int_{-1}^{1} [B_s]^T [D_s][B_s] \det|J|\, d\zeta\, d\eta \right]$$
$$\cdot \begin{bmatrix} \theta_x \\ \theta_y \\ \omega \end{bmatrix} = \begin{bmatrix} M_{\theta_x} \\ M_{\theta_y} \\ f_z \end{bmatrix} \tag{12}$$

3 Plate Infinite Element Method

3.1 Similarity characteristic

As shown in Fig. 3, the basic concept of IEM involves partitioning the computational domain into multiple layers of geometrically-similar elements. For element

I in the upper-most layer, the local nodes are labeled as 1, 2, 3 and 4 in the counterclockwise direction, while the global coordinates of each node are denoted as (x^I, y^I). Taking the origin O as the reference point and assigning the proportionality ratio ξ a value in the interval of $[0,1]$, element II is obtained as shown in Fig. 3 with global coordinates of (x^{II}, y^{II}). The global coordinates of elements I and II are related as follows:

$$(x^{II}, y^{II}) = \xi (x^I, y^I) \tag{13}$$

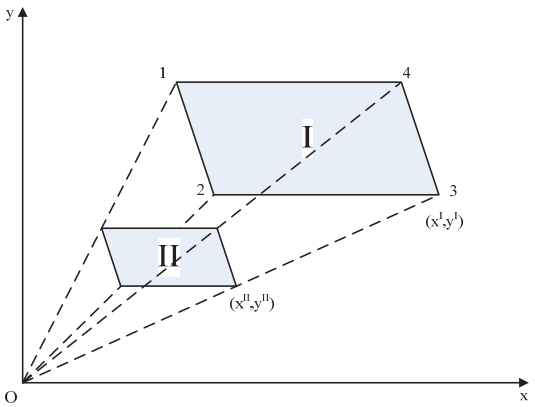

Figure 3: Illustration of the 2-D similar isoparametric elements

The coordinates of any point within element I can be expressed in terms of the nodal coordinates by means of a shape function H_i, as shown in Eqs. (14) and (15). Multiplying both sides of Eqs. (14) and (15) by the proportionality ratio ξ, the coordinates of the corresponding point in element II are obtained as shown in Eqs. (16) and (17), respectively.

$$x^I = \sum_{i=1}^{4} H_i x_i^I \tag{14}$$

$$y^I = \sum_{i=1}^{4} H_i y_i^I \tag{15}$$

$$x^{II} = \xi x^I = \sum_{i=1}^{4} H_i x_i^{II} \tag{16}$$

$$y^{II} = \xi y^I = \sum_{i=1}^{4} H_i y_i^{II} \tag{17}$$

From Eqs. (16) and (17), and recalling Eqs. (8) and (9), it can be shown that:

$$[B_b]_{II} = \frac{1}{\xi}[B_b]_I \tag{18}$$

$$[D_b]_{II} = [D_b]_I \tag{19}$$

$$\det[J]_{II} = \xi^2 \det[J]_I \tag{20}$$

From Eqs. (18) to (20), it is seen that the bending stiffness of the second element layer is the same as that of the first element layer, i.e.,

$$\begin{aligned}
[k_b]_{II} &= \frac{h^3}{12}\int_{-1}^{1}\int [B_b]_{II}^T [D_b]_{II} [B_b]_{II} \det|J|_{II}\, d\zeta\, d\eta \\
&= \frac{h^3}{12}\int_{-1}^{1}\int \frac{1}{\xi}[B_b]_I^T [D_b]_I \frac{1}{\xi}[B_b]_I \xi^2 \det|J|_I\, d\zeta\, d\eta \\
&= \frac{h^3}{12}\int_{-1}^{1}\int [B_b]_I^T [D_b]_I [B_b]_I \det|J|_I\, d\zeta\, d\eta \\
&= [k_b]_I^{-1}
\end{aligned} \tag{21}$$

In adapting the conventional IEM method to Mindler-Reissner plate problems, let the shear stiffness of the first element layer B_s be partitioned into two sub-matrices, $B_s^* \& B_s^{**}$, i.e.,

$$[B_s] = [B_s^*] + [B_s^{**}] \tag{22}$$

$$[B_s^*] = \begin{bmatrix} 0 & 0 & \frac{\partial H_1}{\partial x} & 0 & 0 & \frac{\partial H_2}{\partial x} & 0 & 0 & \frac{\partial H_3}{x} & 0 & 0 & \frac{\partial H_4}{\partial x} \\ 0 & 0 & \frac{\partial H_1}{\partial y} & 0 & 0 & \frac{\partial H_2}{\partial y} & 0 & 0 & \frac{\partial H_3}{y} & 0 & 0 & \frac{\partial H_4}{\partial y} \end{bmatrix} \tag{23}$$

$$[B_s^{**}] = \begin{bmatrix} -H_1 & 0 & 0 & -H_2 & 0 & 0 & -H_3 & 0 & 0 & -H_4 & 0 & 0 \\ 0 & -H_1 & 0 & 0 & -H_2 & 0 & 0 & -H_3 & 0 & 0 & -H_4 & 0 \end{bmatrix} \tag{24}$$

Substituting Eq. (22) into Eq. (7), it follows that

$$k_s = h\kappa \int_{-1}^{1}\int \left[[B_s^*] + [B_s^{**}]\right]^T [D_s] \left[[B_s^*] + [B_s^{**}]\right] \det|J|\, d\zeta\, d\eta \tag{25}$$

Let

$$[S^*] = h\kappa \int_{-1}^{1}\int_{-1}^{1} [B_s^*]^T [D_s][B_s^*] \det|J|\, d\zeta\, d\eta \tag{26}$$

$$[S^{**}] = h\kappa \int_{-1}^{1}\int_{-1}^{1} \{[B_s^*]^T [D_s][B_s^{**}] + [B_s^{**}]^T [D_s][B_s^*]\} \det|J|\, d\zeta\, d\eta \tag{27}$$

$$[S^{***}] = h\kappa \int_{-1}^{1}\int_{-1}^{1} [B_s^{**}]^T [D_s][B_s^{**}] \det|J|\, d\zeta\, d\eta \tag{28}$$

Thus, Eq. (25) becomes

$$k_s = [S^*] + [S^{**}] + [S^{***}] \tag{29}$$

Recalling Eqs. (16) and (17), the relationship between the shear stiffness of element layers *I* and *II* is given as

$$\begin{aligned}[k_s]_{II} &= [S^*]_{II} + [S^{**}]_{II} + [S^{***}]_{II} \\ &= [S^*]_I + \xi[S^{**}]_I + \xi^2[S^{***}]_I \end{aligned} \tag{30}$$

Bring Eq. (21) & Eq. (30) into Eq. (5), the plate stiffness matrix becomes

$$[k]_I = [k_b]_I + [S^*]_I + [S^{**}]_I + [S^{***}]_I \tag{31}$$

$$[k]_{II} = [k_b]_I + [S^*]_I + \xi[S^{**}]_I + \xi^2[S^{***}]_I \tag{32}$$

$$\vdots$$

$$[k]_m = [k_b]_I + [S^*]_I + \xi^{m-1}[S^{**}]_I + \xi^{2(m-1)}[S^{***}]_I \tag{33}$$

3.2 Combined stiffness of PIEM

Figure 4 illustrates the IEM modeling process. The basic steps in the meshing process can be summarized as follows: (1) Discretize the outer boundary Γ_0 using a total of m nodes ordered in the counterclockwise direction. (2) Choose the reference point, O, and using the specified proportionality constant, ξ, automatically construct multiple similar curves $\Gamma_1, \Gamma_2, \ldots, \Gamma_s$ of Γ_0 centered at reference point O with proportionality constants $\xi^1, \xi^2, \ldots, \xi^s$, respectively. Note that s denotes the number of element layers (specified in advance). Let the region bounded by curves Γ_{i-1} and Γ_i be denoted as the ith element layer $(i = 1, 2, 3, \ldots, s)$. (3) Regularly discretize each element layer Γ_i using the same number of nodes as that used for

layer Γ_0 and determine the coordinates of each node using Eq. (13). Each layer elements are meshed automatically into four nodes quadrilateral elements in a radial direction.

The stiffness matrix of the upper-most element layer has the form shown in Eq. (34), where k_a, k_b and A are the sub-matrices of the stiffness matrix.

$$k_1 = \begin{bmatrix} [k_a]_1 & [-A]_1^T \\ [-A]_1 & [k_b]_1 \end{bmatrix} \tag{34}$$

Substituting Eq. (34) into Eq. (12) and expanding, the stiffness matrices of the s element layers in the computational domain are obtained as follows:

$$\begin{bmatrix} [k_a]_1 & [-A]_1^T \\ [-A]_1 & [k_b]_1 \end{bmatrix} \cdot \begin{Bmatrix} \delta_0 \\ \delta_1 \end{Bmatrix} = \begin{Bmatrix} f_0 \\ f_1 \end{Bmatrix} \tag{35}$$

$$\vdots$$

$$\begin{bmatrix} [k_a]_i & [-A]_i^T \\ [-A]_i & [k_b]_i \end{bmatrix} \cdot \begin{Bmatrix} \delta_{i-1} \\ \delta_i \end{Bmatrix} = \begin{Bmatrix} -f_{i-1} \\ f_i \end{Bmatrix} \tag{36}$$

$$\vdots$$

$$\begin{bmatrix} [k_a]_s & [-A]_s^T \\ [-A]_s & [k_b]_s \end{bmatrix} \cdot \begin{Bmatrix} \delta_{s-1} \\ \delta_s \end{Bmatrix} = \begin{Bmatrix} -f_{s-1} \\ f_s \end{Bmatrix} \tag{37}$$

where δ_i is the nodal displacement vector associated with element layer Γ_1 and f_i is the corresponding nodal force vector. Note that Γ_i and f_i are defined respectively as

$$\delta_i = [\theta_{x1}^i \theta_{y1}^i \omega_1^i \dots \theta_{xm}^i \theta_{ym}^i \omega_m^i]^T \tag{38}$$

$$f_i = [M_{x1}^i M_{y1}^i f_{z1}^i \dots M_{xm}^i M_{ym}^i f_{zm}^i]^T \tag{39}$$

Keep the first and last equation of Eq. (35) and Eq. (37), and combine the second equation for the ith element-layer and the first equation for the $(i+1)$th element-layer. Assuming that no internal force is applied to Γ_s(i.e., $f_s = 0$), Eqs. (35) to (37) become

$$[k_a]_1 \cdot \delta_0 - [A]_1^T \cdot \delta_1 = f_0 \tag{40}$$

$$\vdots$$

$$-[A]_i^T \cdot \delta_{i-1} + [[k_b]_i + [k_a]_{i+1}] \cdot \delta_i - [A]_{i+1}^T \cdot \delta_{i+1} = 0 \tag{41}$$

$$\vdots$$

$$-[A]_s \cdot \delta_{s-1} + [k_b]_s \cdot \delta_s = 0 \tag{42}$$

Let

$$[M]_s = [k_b]_s \tag{43}$$

$$\vdots$$

$$[M]_i = [[k_b]_i + [k_a]_{i+1}] - [A]_{i+1}^T \cdot [M]_{i+1}^{-1} \cdot [A]_{i+1} \tag{44}$$

$$\vdots$$

$$[M]_1 = [[k_b]_1 + [k_a]_2] - [A]_2^T \cdot [M]_2^{-1} \cdot [A]_2 \tag{45}$$

Since $[M]_s$ is equal to known $[k_b]_s, [M]_{s-1}, [M]_{s-2}, \ldots, [M]_2$, and $[M]_1$ can be calculated iteratively by means of Eqs. (43) to (45). Finally, substituting Eq. (48) into Eq. (40), the combined stiffness matrix $k_{IEM} = \{[k_a]_1 - [A]_1^T \cdot [M]_1^{-1} \cdot [A]_1\}$ is obtained with the form shown in Eq. (49). In other words, all of the inner elements layers are combined to form a single super-element with master nodes at the outer boundary Γ_0 only.

$$\delta_s = [M]_s^{-1} \cdot [A]_s \cdot \delta_{s-1} \tag{46}$$

$$\vdots$$

$$\delta_i = [M]_i^{-1} \cdot [A]_i \cdot \delta_{i-1} \tag{47}$$

$$\vdots$$

$$\delta_1 = [M]_1^1 \cdot [A]_1 \cdot \delta_0 \tag{48}$$

$$\{[k_a]_1 - [A]_1^T \cdot [M]_1^{-1} \cdot [A]_1\} \cdot \delta_0 = f_0 \tag{49}$$

Ying [Ying (1995)] proved that k_{IEM} converges toward a certain constant quantity as the number of element layers approaches infinity, i.e.,

$$\lim_{s\to\infty} k_{IEM}^{(s)} = k_{IEM} \tag{50}$$

where s denotes the number of the defined element layers. However, Eq. (50) could not be directly applied to the numerical formulation due to the infinity element layers is not countable in a physical sense. Therefore, Liu [Liu and Chiou (2003)] proposed a convergence method to observe the diagonal trace terms $k_{IEM}^{(s)}(j,j)$. When the desired accuracy criteria $\varepsilon = \left| \frac{k_{IEM}^{(i+1)}(j,j) - k_{IEM}^{(i)}(j,j)}{k_{IEM}^{(i+1)}(j,j)} \right| \times 100\% \leq 10^{-6}$ is satisfied, the iterative program is terminated and the critical element layers number, "S_{cr}", is determined as equal to the terminated iterative value, "i". S_{cr} is the minimum element layers needed for the convergence; this implies that there are enough elements to

cover the entire domain. The proportionality ratio ξ is another important factor in the convergence study. Basically, the greater ξ is chosen, the more S_{cr} is needed. In other words, given a sufficiently large value of s, the stiffness $k_{IEM}^{(s)}$ is approximately equal to the combined stiffness k_{IEM}.

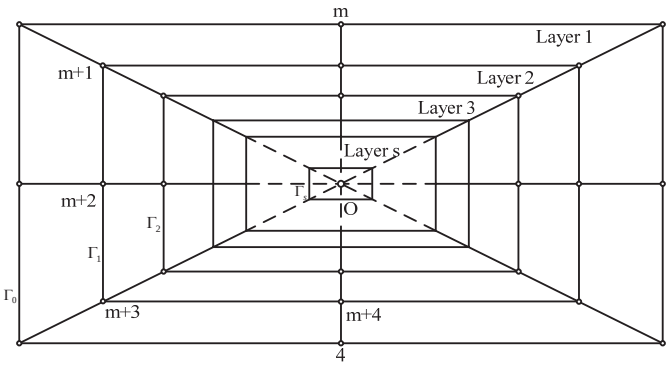

Figure 4: IEM mesh and reference point

3.3 Integration of IEM and FEM schemes

Meshing the entire computational domain using the IEM scheme is not favorable when the body of interest has a concave or complex characteristic. Accordingly, the present study constructs a combined PIEM/FEM scheme in which the region of the computational domain containing the singularity (i.e., a through-thickness hole in the present case) is meshed using the PIEM scheme, while the remainder of the domain is meshed using the conventional FEM scheme. As shown in Fig. 5, the two regions of the domain are denoted as Π and Ω, respectively, and are connected by a coupling interface Γ_0 comprising common nodes, δ_0. Note that the common nodes are converted directly from the original master nodes on the boundary region of the IE domain. Liu [Liu and Chiou (2003)] showed that the stiffness matrix for the combined IEM/FEM domain has the form

$$\begin{bmatrix} k_{coupled}+k_{IEM} & k_{cf}^T \\ k_{cf} & k_{FEM} \end{bmatrix} \cdot \begin{Bmatrix} \delta_0 \\ \delta_{FEM} \end{Bmatrix} = [k_{IE-FE}] \cdot \begin{Bmatrix} \delta_0 \\ \delta_{FEM} \end{Bmatrix} = \begin{Bmatrix} 0 \\ f_{FEM} \end{Bmatrix} \tag{51}$$

where δ_0 and δ_{FEM} are the displacement vectors of the interface and non-interface nodes, respectively; f_{FEM} is the associated loading force vector; and k_{IE-FE} is the global system stiffness matrix.

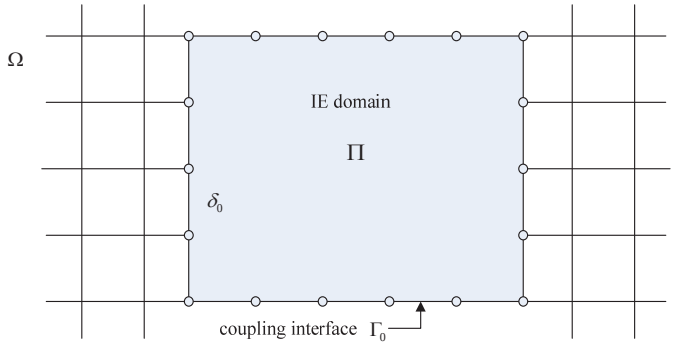

Figure 5: Combined PIEM / FEM mesh of computational domain

4 Numerical Examples

In this section, the validity of the proposed PIEM algorithm is demonstrated by comparing the results obtained for the deflection of a plate under 4PB testing with those obtained using conventional ABAQUS Finite Element Method (FEM) software [Hibbitt, Karlsson, and Sorensen (2004)]. The combined PIEM/FEM scheme is then used to investigate the effects of the hole size, hole position and hole profile / area on the bending strength (flexural rigidity) of simply-supported rectangular plates containing a single through-thickness hole. (Note that the PIEM/FEM scheme is programmed using MATLAB software [Kwon and Bang (2000)].)

4.1 Validation of PIEM algorithm

Consider the rectangular plate shown in Fig. 6 with dimensions of $100mm \times 50mm \times 0.5mm$ (length×width×thickness). Assume that two of the opposite edges are simply supported (i.e., $\omega = 0$), while the other two edges are free such that the applied bending moment ($M = 100N - mm$) vanishes along the two simply-supported edges. Assume also that the plate has a Young's Modulus of $E = 200GPa$ and a Poisson ratio of $v = 0.30$. Figure 7 presents the corresponding PIEM mesh pattern before the mesh is degenerated to form a single super-element.

Figure 8 shows the results obtained for the bending displacement of the plate using commercial ABAQUS FEM software. Meanwhile, Fig. 9 compares the results obtained for the deflection profile of edge $\overline{AE}$ of the plate (see Fig. 6) using the proposed PIEM scheme with those obtained via the FEM method. Note that in implementing the PIEM scheme, the proportionality ratio is assigned various values in the range of $\xi = 0.5 \sim 0.9$, while the number of element layers is specified in the range of $s = 10 \sim 50$. As mentioned in the Section 3, the greater ξ is chosen,

the more s is need. Otherwise, the void will exist around the reference point in the plate and reduce the plate stiffness. Therefore, the maximum deflection increases rapidly under the improper setting (e.g., $\xi = 0.9, s = 10$).

The detail PIEM, ABAQUS result and relative difference (RD) estimate are provided in the Tab. 1. It is seen that a good agreement is observed when the proportionality ratio and number of element layers are specified as $\xi = 0.9$ and $s = 50$, respectively. The RD reduce from 126.504 % ($\xi = 0.95$, $s = 10$) to 0.016 % ($\xi = 0.9$, $s = 50$). Thus, the basic validity of the proposed PIEM algorithm is confirmed. In addition, it is observed that the accuracy of the PIEM scheme improves as ξ and s increase.

Table 2 shows the comparisons of PIEM and FEM by execution time and number of DOFs on an Intel Core-4.0 GHz computer. For the PIEM solver, the execution time is only 0.254s, whereas, the execution time for the similar mesh configuration using FEM is 1.8s. The present method reduces by about 85.88% the execution time when compared with that of full FEM. Similarly, the complicated models are more significant. This is due to the fact that number of DOFs of the PIEM model is much fewer.

Accordingly, in performing the remaining simulations, the proportionality ratio and number of element layers were specified as $\xi = 0.9$ and $s = 50$, respectively.

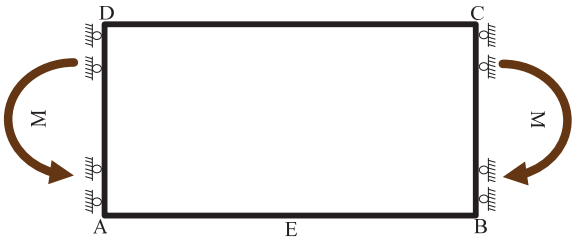

Figure 6: Simply-supported rectangular plate subject to 4BP testing

Table 1: Maximum deflection (*mm*) by PIEM in variation of proportionality ratios ξ with specified element layers

ξ \ s	10		20		30		40		50	
	Max. deflection	RD (%)	Max. deflection	RD (%)	Max. deflection	RD (%)	Max. deflection	RD (%)	Max. deflection	RD (%)
0.5	1.1169	9.423	1.1167	9.439	1.11669	9.440	1.11669	9.440	1.1167	9.439
0.6	1.17229	4.931	1.17218	4.940	1.1722	4.938	1.1722	4.938	1.1722	4.938
0.7	1.20743	2.081	1.20533	2.251	1.20534	2.250	1.20534	2.250	1.20534	2.250
0.8	1.25766	1.993	1.2243	0.713	1.2239	0.745	1.2239	0.745	1.2239	0.745
0.9	1.63912	32.928	1.27733	3.588	1.23824	0.418	1.23349	0.032	1.23289	0.016
0.95	2.793	126.504	1.66826	35.291	1.37839	11.783	1.28483	4.196	1.25257	1.580
Max. deflection of ABAQUS is 1.23309 *mm*										

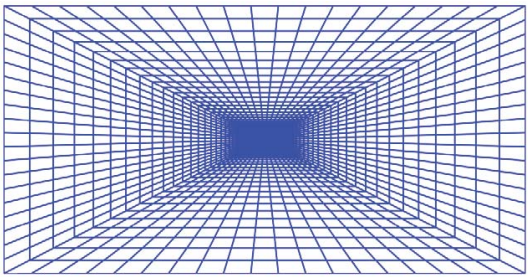

Figure 7: Complete IEM mesh of simply-supported rectangular plate

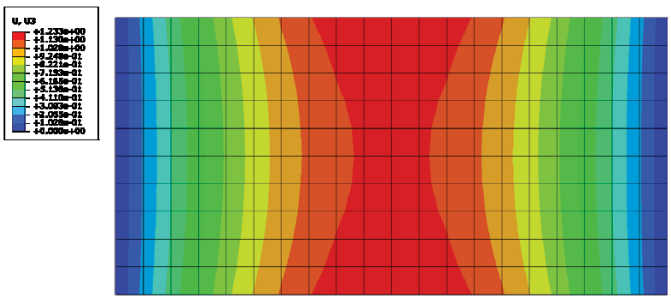

Figure 8: ABAQUS solution for deflection contour profile of simply-supported rectangular plate

Table 2: Execution time and DOFs of the PIEM and FEM approaches

Numerical method	Execution time (s)	PIEM master nodes	PIEM layers	Total nodes	Total DOFs	Equivalent DOFs
PIEM	0.254	60	50	60	180	9000
FEM (ABAQUS)	1.800	-	-	3042	9126	9126

4.2 Application of proposed PIEM / FEM scheme

Consider the rectangular plate shown in Fig. 10 containing a single through-thickness hole in the center-point position and subject to four-point bending. Assume that the region of the plate surrounding the hole is meshed using the proposed PIEM scheme, while the remainder of the plate is meshed using the FEM scheme. Thus, in investigating the effects on the bending strength of changes in the hole characteristics (e.g., position, size and profile / area), it is necessary only to re-mesh the PIEM region of the computational domain and to substitute the combined stiffness of the IEM element into the global stiffness matrix.

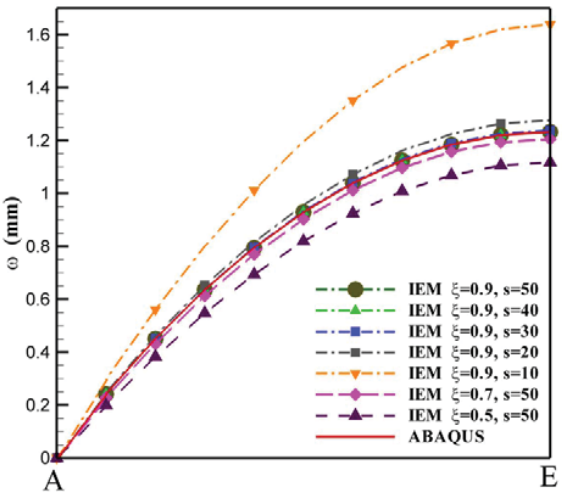

Figure 9: Comparison of ABAQUS and PIEM solutions for edge deflection of simply-supported rectangular plate

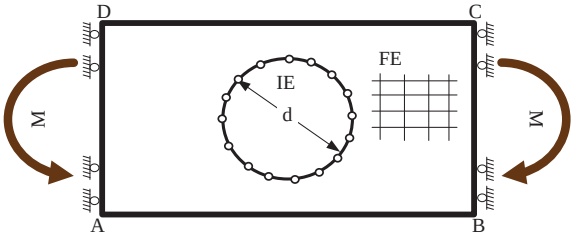

Figure 10: Combined PIEM/FEM mesh of simply-supported rectangular plate subject to 4PB testing

4.3 Example 1: effect on bending strength of hole diameter and plate thickness

Assume that the rectangular plate has a length of 100 *mm*, a width of 50 *mm* and a thickness in the range of $0.2 \sim 0.5mm$. Assume also that the through-thickness hole has a diameter in the range of $0 \sim 40mm$. Figure 11 presents the results obtained using the combined PIEM/FEM scheme for the variation of the flexural stiffness of the plate (S_b) with the hole diameter as a function of the plate thickness. As expected, the results show that the flexural stiffness reduces rapidly with a reducing plate thickness. Moreover, it is seen that the flexural stiffness reduces as the hole diameter increases; particularly at higher values of the plate thickness.

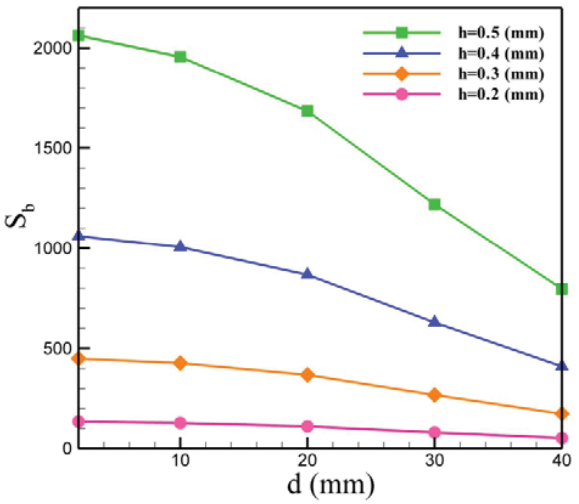

Figure 11: Variation of flexural stiffness with through-thickness hole diameter as function of plate thickness

4.4 Example 2: effect on bending strength of hole position

Assume that the through-thickness hole is located at various x- and y-axis positions of the plate, as shown in Fig. 12. Assume also that the plate has dimensions of 100 mm x 50 mm x 0.2 (length×width×thickness). Figures 13 and 14 show the variation of the flexural stiffness with the x- and y-axis positions of the hole, respectively, as a function of the hole diameter. In general, the results show that the flexural stiffness reduces as the hole location moves toward the upper central region of the plate (i.e., the point of maximum deformation).

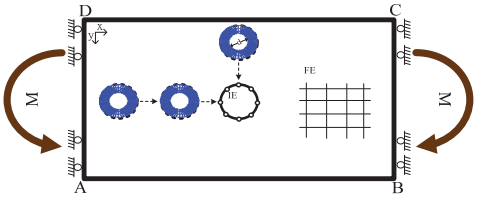

Figure 12: Schematic illustration showing rectangular plate containing through-thickness holes in various x- and y-axis positions

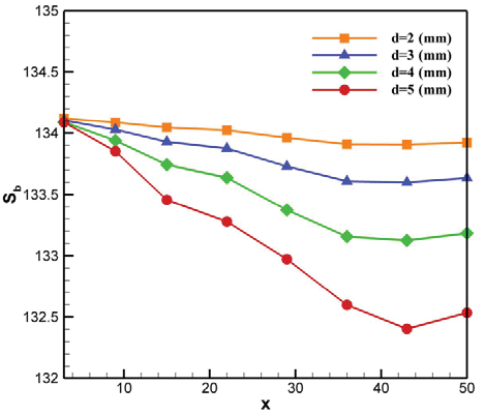

Figure 13: Variation of flexural stiffness with x-axis position of through-thickness hole as function of through-hole diameter

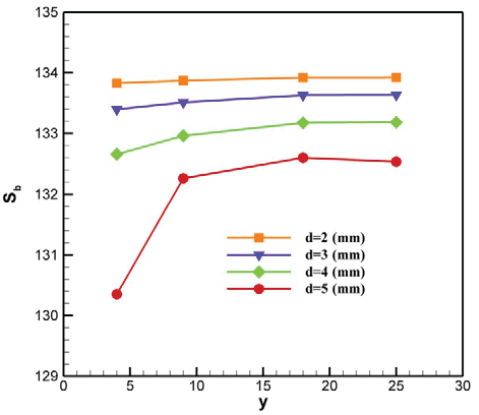

Figure 14: Variation of flexural stiffness with y-axis position of through-thickness hole as function of through-hole diameter

4.5 Example 3: effect on bending strength of hole profile / area

Assume that the plate considered in the previous examples contains a single elliptical hole in the center-point position. As shown in Fig. 15, let the major axis of the hole be denoted as $2a$, the minor axis be denoted as $2b$, and the edge angle (i.e., the angle between the major axis and the horizontal axis) be denoted as θ. The analysis considers four different elliptical holes. As shown in Tab. 3, the major and minor axis lengths of elliptical hole 1 ($E1$) are defined in such a way that the area of the hole is identical to that of a circular hole with a diameter of 20 *mm*. Meanwhile,

the axis lengths of the remaining elliptical holes are specified in such a way that the corresponding areas are equal to 0.8, 0.6 and 0.4 times the area of the circular hole, respectively. Figure 16 shows the variation of the flexural stiffness with the edge angle for each of the four considered elliptical holes. It is seen that the flexural stiffness reduces significantly as the major axis of the elliptical hole rotates towards 90° (i.e., parallel to the bending moment M); particularly as the hole size increases.

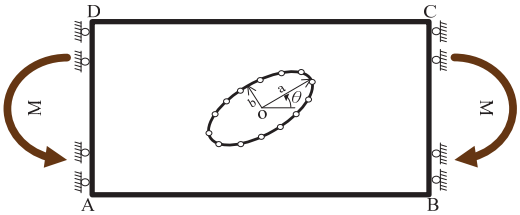

Figure 15: Schematic illustration showing simply-supported rectangular plate with elliptical hole subject to 4PB testing

Table 3: Areas of four considered elliptical holes relative to area of circular hole with diameter of $d = 20mm$

Shape	Circular	$E1$	$E2/E1$	$E3/E1$	$E4/E1$
Area	$\pi \times 10 \times 10$	$\pi \times 20 \times 5$	0.8	0.6	0.4

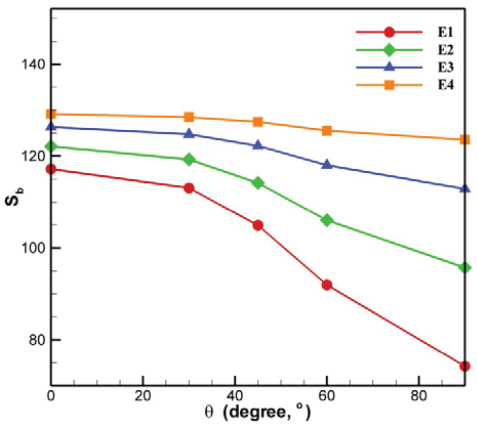

Figure 16: Variation of flexural rigidity with edge angle of elliptical hole as function of hole area

5 Conclusion

In Mindlin-Reissner plate bending problems, the conventional IEM formulation cannot be directly applied due to the incompatible differential order of the shear stiffness component. Accordingly, the present study has proposed a Plate IEM (PIEM) scheme in which the shear element stiffness matrix is decomposed into two shear stiffness sub-matrices (k_b and k_s) such that each sub-matrix is similar to the equivalent sub-matrix in all of the other element layers in the discretized domain. The validity of the proposed scheme has been demonstrated by comparing the results obtained for the deflection of a simple plate under 4PB testing with those obtained using conventional ABAQUS FEM software. The PIEM scheme has been combined with the conventional FEM scheme and used to analyze the effect of the through-thickness hole size, position and profile/area on the bending strength of a rectangular plate under 4PB testing. In combining the two schemes, the region of the computational domain containing the hole is meshed using the PIEM scheme, while the remainder of the domain is meshed using the FEM method. The combined PIEM/FEM method enables the effects of the hole size, hole position and hole profile/area to analyzed by simply re-meshing the PIEM region of the domain and then updating the combined stiffness of the corresponding super-element in the global stiffness matrix accordingly. In other words, the computational efficiency of the proposed scheme is significantly higher than that of the conventional FEM method, in which the entire domain must be re-meshed each time a change in the through-thickness hole properties occurs. In general, the results presented in this study have shown that the proposed PIEM/FEM scheme provides an easily-implemented, computationally-efficient and accurate means of analyzing various common engineering plate bending problems.

Acknowledgement: The authors gratefully acknowledge the financial support provided to this study by the National Science Council of Taiwan, R. O. C., under Grant Nos. NSC 101-2221-E-194-014-MY3 and NSC 101-2923-E-194-002-MY3.

References

Chen, J. T.; Hsiao, C. C.; Leu, S. Y. (2006): Null-field integral equation approach for plate problems with circular boundaries. *ASME Journal of Applied Mechanics*, vol. 73, no. 4, pp. 679–693.

Chen, J. T.; Shen, W. C.; Chen, P. Y. (2006): Analysis of circular torsion bar with circular holes using null-field approach. *CMES: Computer Modeling in Engineering & Sciences*, vol. 12, no. 2, pp. 109–119.

Cui, X. Y.; Liu, G. R.; Li, G. Y. (2010): Analysis of mindlin-reissner plates using cell-based smoothed radial point interpolation method. *International Journal of Applied Mechanics*, vol. 2, no. 3, pp. 653–680.

Dong, C. Y.; Lo, S. H.; Cheung, Y. K. (2004): Numerical solution for elastic half-plane inclusion problems by different integral equation approaches. *Engineering Analysis with Boundary Elements*, vol. 28, pp. 123–140.

Feraboli, P.; Kedward, K. T. (2003): Four-point bend interlaminar shear testing of uni- and multi-directional carbon/epoxy composite systems. *Composites: Part A: Applied Science and Manufacturing*, vol. 34, pp. 1265–1271.

Hibbitt, D.; Karlsson, B.; Sorensen, P. (2004): *ABAQUS User's Manual Version 6.5*. Pawtucket, RI.

Huurman, M.; Gelpke, R.; Jacobs, M. J. (2012): A theoretical investigation into the 4 point bending test. In *7th RILEM International Conference on Cracking in Pavements*, pp. 475–486.

Kee, B. T.; Liu, G. R.; Lu, C. (2008): A least-square radial point collocation method for adaptive analysis in linear elasticity. *Engineering Analysis with Boundary Elements*, vol. 32, pp. 440–460.

Komur, M. A.; Sonmez, M. (2008): Elastic buckling of rectangular plates under linearly varying in-plane normal load with a circular cutout. *Mechanics Research Communications*, vol. 35, pp. 361–371.

Kwon, Y. W.; Bang, H. (2000): *The Finite Element Method using MATLAB*. CRC Press, New York, 2nd edition.

Lee, M. H.; Park, J. M. (2004): Flexural stiffness of selected corrugated structures. *Packaging Technology and Science*, vol. 17, pp. 275–286.

Lee, W. M.; Chen, J. T.; Lee, Y. T. (2007): Free vibration analysis of circular plates with multiple circular holes using indirect biems. *Journal of Sound and Vibration*, vol. 304, pp. 811–830.

Liu, D. S.; Chiou, D. Y. (2003): A coupled iem/fem approach for solving elastic problems with multiple cracks. *International Journal of Solids and Structures*, vol. 40, pp. 1973–1993.

Liu, D. S.; Chiou, D. Y. (2004): 2-d infinite element modeling for elastostatic problems with geometric singularity and unbounded domain. *Computers & Structures*, vol. 83, pp. 2086–2099.

Liu, D. S.; Tu, C. Y.; Chung, C. L. (2012): Eigenvalue analysis of mems components with multi-defect using infinite element method algorithm. *CMC: Computers, Materials & Continua*, vol. 28, no. 2, pp. 97–120.

Liu, G. R.; Chen, X. L. (2001): A mesh-free method for static and free vibration analyses of thin plates of complicated shape. *Journal of Sound and Vibration*, vol. 241, pp. 839–855.

Maiorana, E.; Pellegrino, C.; Modena, C. (2009): Elastic stability of plates with circular and rectangular holes subjected to axial compression and bending moment. *Thin-Walled Structures*, vol. 41, pp. 241–255.

Mindlin, R. D. (1951): Influence of rotatory inertia and shear on flexural motions of isotropic, elastic plates. *ASME Journal of Applied Mechanics*, vol. 18, pp. 31–38.

Nguyen-Xuan, H.; Rabczuk, T.; Bordas, S.; Debongnie, J. F. (2008): A smoothed finite element method for plate analysis. *Computer Methods in Applied Mechanics and Engineering*, vol. 197, pp. 1184–1203.

Park, J.; Kim, G.; Kwon, S.; Chung, S. (2012): Finite element analysis of corrugated board under bending stress. *Journal of the Faculty of Agriculture, Kyushu University*, vol. 57, pp. 181–188.

Wang, C. M.; Lim, G. T.; Reddy, J. N.; Lee, K. H. (2001): Relationships between bending solutions of reissner and mindlin plate theories. *Engineering Structures*, vol. 23, pp. 838–849.

Yamamoto, N.; Hongo, M.; Berglund, L. J.; Sperling, J. W.; Cofield, R. H.; An, K. N.; Steinmann, S. P. (in press): Biomechanical analysis of a novel locking plate with smooth pegs versus a conventional locking plate with threaded screws for proximal humerus fractures. *Journal of Shoulder and Elbow Surgery*.

Yang, Z.; Kim, C. B.; Cho, C.; Beom, H. G. (2008): The concentration of stress and strain in finite thickness elastic plate containing a circular hole. *International Journal of Solid and Structures*, vol. 45, pp. 713–731.

Ying, L. A. (1992): An introduction to infinite element method. *Mathematics in Practice Theory*, vol. 2, pp. 69–78.

Ying, L. A. (1995): *Infinite Element Method*. Peking University Press, Beijing, and Vieweg Publishing.

Yu, P.; Guo, W.; She, C.; Zhao, J. (2008): The influence of poisson's ratio on thickness-dependent stress concentration at elliptic holes in elastic plates. *International Journal of Fatigue*, vol. 30, pp. 165–171.